

A comparative braking scheme in auto-electric drive systems with permanent magnet synchronous machine

Crescent Onyebuchi Omeje¹, Candidus Ugwuoke Eya²

¹Department Electrical Electronic Engineering, Faculty of Engineering, University of Port Harcourt, Port Harcourt, Nigeria

²Department Electrical Engineering, Faculty of Engineering, University of Nigeria, Nsukka, Nigeria

Article Info

Article history:

Received Aug 12, 2022

Revised Oct 20, 2022

Accepted Oct 27, 2022

Keywords:

Field oriented control
IPMSM
Mathematical modeling
MRPP
MRPP-torque
Regenerative braking
SMPM
Three-level VSI

ABSTRACT

Permanent magnet synchronous machines (PMSMs) are gaining popularity due to renewable energy and the electrification of transportation. Permanent magnet synchronous machines are receiving interest because of their great dependability, low maintenance costs, and high-power density. This research compares surface mounted permanent magnet (SMPM) with interior permanent magnet (IPM) synchronous machines using MATLAB. Mathematical models and simulation analyses of two permanent magnet synchronous machines under regenerative braking are presented. Maximum regeneration power point (MRPP) and torque (MRPP-torque) for two machine types were simulated at variable electrical speed and q-axis current. Simulation results showed IPMSM produced more output power due to saliency than SMPM at varying speed and current with higher MRPP and MRPP-Torque. Simulation was used to compare the dynamic impacts of constant and variable braking torques on an auto-electric drive's speed and produced torque on a plain surface and a sloppy driving plane. 81.68% and 74.95% braking efficiency were measured on level ground and a sloppy plane, respectively. Simulations indicated that lithium-ion battery state of charge varied linearly with constant braking torque and exponentially with varying braking torque, reflecting efficiency values. All simulations were in MATLAB/Simulink 2014.

This is an open access article under the [CC BY-SA](https://creativecommons.org/licenses/by-sa/4.0/) license.



Corresponding Author:

Crescent Onyebuchi Omeje
Department Electrical Electronic Engineering, Faculty of Engineering, University of Port
Port Harcourt, Nigeria
Email: crescent.omeje@uniport.edu.ng

1. INTRODUCTION

The inherent environmental challenges and sporadic energy dissipations associated with fossil fuel operated automobiles have drawn much needed attentions to the evolution of new energy saving vehicles that is environmentally benign. To achieve the proposed plan for sustainable development (SD) on climate change, energy availability and affordability is crucial. Though concerted effort is being made by several nations around the world towards the search for sustainable and renewable energy (RE) source that will supplement the energy requirements with due considerations to factors such as the increasing demand for energy, the decline in fossil fuel reserves, CO₂ reduction and global climate change [1].

The necessities of adopting battery operated electric vehicles with the obvious advantages of high efficiency and zero gas emissions have intensively been researched upon and implemented in most automotive industries. This method appears to have its specific limitations which are embedded in the driving range and cost of battery size [2]. These limitations have been addressed through the regenerative braking process and energy recycling method as referenced in [3]. During a regenerative braking process, the electric

automobile operates as a generator and releases electrical energy that is recycled to charge the batteries of the electric vehicle through a power electronic bidirectional converter [4]. A hybrid energy storage system (HESS) by composition is made up of energy recharged batteries with ultra-capacitor bank. This has been adopted to significantly improve the driving range limitations of most electric automobiles [5].

Regenerative braking has a great advantage to electric vehicles than the conventional vehicles. Kinetic energy usually is been recovered to energy storage devices than been wasted as heat [6], [7]. At low-speed range where insufficient braking torque is delivered, plug braking becomes very essential however energy is drawn out of the battery instead of being recovered in the process [8]. In recent time, high performance with proven high density powered permanent magnet synchronous machine is been deployed as a major traction motor in the drive system of most electric vehicles [9]. A major concern in permanent magnet synchronous machines (PMSM) design is traced to the nature and type of permanent magnet material used. Neodymium iron-boron (Nd₂Fe₃B) stands as the finest option with regard to its excellent B-H characteristic though its high cost and limited supply poses a challenge [10].

IPMSM and SMPM forms the two main types of permanent magnet synchronous machine obtainable with respect to the placement of the magnets on the rotor. SMPM has its magnet mounted directly at the surface which makes it adaptable to low-speed application. The motor has equal inductance which implies that the d-axis inductance is equal to the q-axis inductance ($L_d=L_q$) and therefore the saliency is entirely zero [11]. SMPM power output is relative to the magnetic excitation. The interior permanent magnet machine has its magnet positioned inside the rotor and is applied in high-speed operation. The motor has saliency since quadrature-axis inductance is always greater than the direct-axis inductance ($L_q>L_d$). Hence, presence of saliency results in an appreciable cumulative power output than the SMPM. Figures 1(a) and 1(b) present the magnet arrangement in the rotor of IPMSM and SMPM.

This paper is structured as follows: Section 1 the introductory section; Section 2 is reviewed literature of related work; Section 3 is the research methods which enumerated the mathematical models of the machine showing the maximum regenerative power point MRPP and MRPP-Torque; Section 4 presents the simulation results while part V is the conclusions and recommendations.

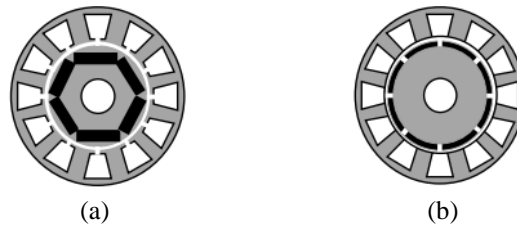


Figure 1. The structure of (a) IPMSM and (b) SPMSM

2. RELATED WORKS

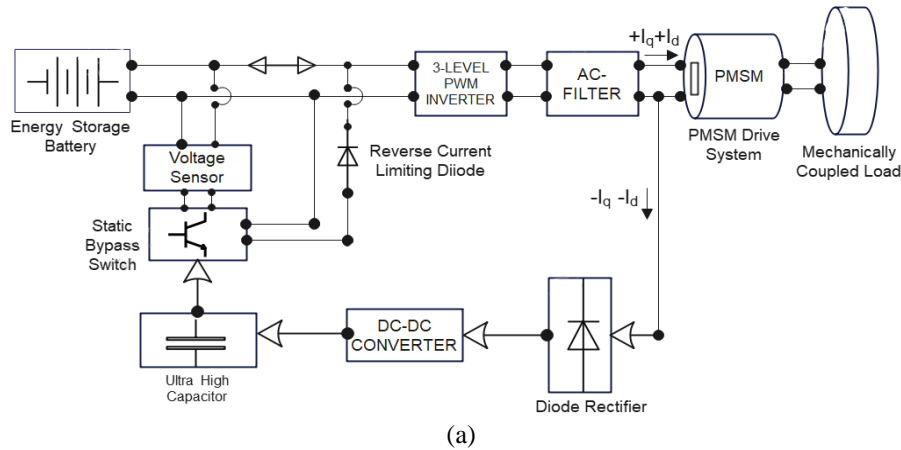
Currently, most electric vehicles are basically designed on the principles of regenerative braking which imply converting a seemingly lost energy during brake back into the battery via the power inverter. A compact regenerative braking scheme for electric automobiles development was presented in [12]. Research work carried out in [13], discussed the regenerative braking, modeling and control of the machine in extreme condition. In [14], a combined three torque control methods in regenerative braking design was elaborated. Some published research works have dwelt on the system braking design of electric motors based on short-circuit braking which converts motor back-EMF directly to braking torque [15], [16]. Though this technology is applied to electric bicycles and motorcycles, its speed limitation and losses makes it very inefficient. The short circuit braking is another approach which can be amended through a reverse field brake with rheostat. This method can be applied at any speed as proposed in [17]. The maximum torque per ampere (MTPA) control is adopted as the preferred control method applied in driving the IPMSM in electric vehicle due to the high torque capability at low speed and wide speed range as reported in [18]. The significance of maximum torque per ampere (MTPA) control method is to trace the minimum current vector that gives the required torque and current which also provides the maximum constant torque as given in [19].

In this paper, the electrical braking torque and maximum regenerative power produced by the two selected permanent magnet synchronous machines (IPMSM and SMPM) were modelled and simulated at varying load current and motor speed. The dynamic effects at a constant and varying braking torques of the auto-electric drive on a plain surface and on a slopy driving plane in terms of speed and developed torque were also considered through simulation. The variations in the lithium-ion battery state of charge under a constant braking torque and under a varying braking torque was also assessed through simulation. Efficiency

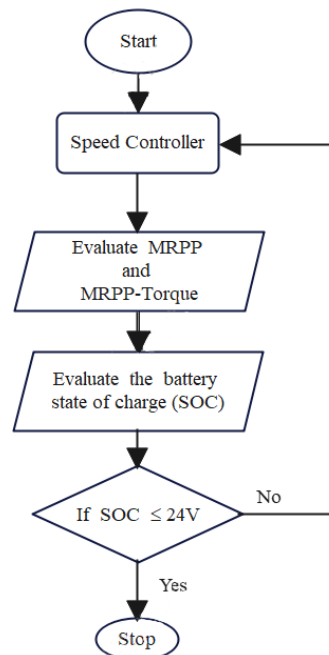
values of 81.68% and 74.95% were obtained during braking at a constant torque on level ground and at a varied torque on a sloppy plane. The variation in efficiency is indicative of more energy dissipation on a sloppy plane.

3. METHOD

Braking process generally can either be classified as a constant speed braking or variable speed braking depending on the driving state arrangement. A constant speed braking is frequently applied in the plain sailing driving while the variable speed braking often occurs on a swift slowing down process [20]. In both processes energy is either regenerated or recycled in a storage scheme. General hybrid energy storage scheme in electric vehicle is shown in Figure 2(a) while the flow chart algorithm for the control operation of the electric vehicle in terms of regenerative braking and battery state of charge is presented in Figure 2(b).



(a)



(b)

Figure 2. A hybrid energy storage scheme: (a) block diagram of battery-ultra high capacitor hybrid energy storage system and (b) flow chart of battery powered electric vehicle

Basic operations of the HESS-system presented in Figure 2(a) are illustrated in three modes as presented:

- Normal mode: In this mode, PMSM mechanically coupled load is fed through the battery supplied PWM inverter scheme while the ultra-high capacitor is been charged in the process.

- Outage mode: During a drop in the battery voltage as indicated by the voltage sensor, the ultra-capacitor is propelled to provide the required energy to the PWM inverter through the static switch as an ancillary measure for energy boost.
- Regenerative braking mode: When there is an electrical brake in speed with maximum energy recovery, the battery regains its voltage and supplies the required voltage to the PWM inverter thereby maintaining a continuous operation.

Electric braking based on field-oriented control (FOC) is achieved by applying a q-axis current in the negative polarity to the braking torque or by controlling the motor speed to track a ramp reference that progressively get to zero [21]. Maximum regenerative power point (MRPP) of SMPM and IPMSM for a given motor speed is derived directly from the conventional voltage and power equations. Voltage equation of the SMPM with the same inductance ($L_d = L_q$) under dynamic state operation is given by (1).

$$\begin{bmatrix} V_d^e \\ V_q^e \end{bmatrix} = \begin{bmatrix} R_s + SL_s & -L_s \omega_e \\ L_s \omega_e & R_s + SL_s \end{bmatrix} \begin{bmatrix} i_d \\ i_q \end{bmatrix} + \begin{bmatrix} 0 \\ \omega_e \psi_f \end{bmatrix} \quad (1)$$

Motor active electrical power is made up of copper loss and dynamic power which is given by (2).

$$P_{e-SPMSM} = \frac{3}{2} (R_s i_q^2 + \omega_e \psi_f i_q) \quad (2)$$

The maximum regenerative power point (MRPP) current can be obtained by setting the derivative of (2) to zero.

$$\frac{dP_{e-SPMSM}}{di_q} = \frac{3}{2} (2R_s i_q + \omega_e \psi_f) \quad (3)$$

$$\frac{dP_{e-SPMSMmin}}{di_q} = \frac{3}{2} (2R_s i_q + \omega_e \psi_f) = 0 \quad (4)$$

The MRPP current in terms of motor speed and flux linkage is therefore given by (5).

$$i_{qmin} = \frac{-\psi_f \omega_e}{2R_s} \quad (5)$$

Similarly, the maximum regenerative power is obtained by substituting in (5) into (2).

$$P_{e-MRPP} = \frac{3}{2} (R_s i_{qmin}^2 + \omega_e \psi_f i_{qmin}) = \frac{3}{2} \left(\frac{\psi_f^2 \omega_e^2}{4R_s} - \frac{\psi_f^2 \omega_e^2}{2R_s} \right) = \frac{-3\psi_f^2 \omega_e^2}{8R_s} \quad (6)$$

Dynamic voltage equation of IPMSM with different dq-axis inductance ($L_d \neq L_q$) is given by (7).

$$\begin{bmatrix} V_d^e \\ V_q^e \end{bmatrix} = \begin{bmatrix} R_s + SL_d & -L_q \omega_e \\ L_d \omega_e & R_s + SL_q \end{bmatrix} \begin{bmatrix} i_d \\ i_q \end{bmatrix} + \begin{bmatrix} 0 \\ \omega_e \psi_f \end{bmatrix} \quad (7)$$

Motor active electrical power for the IPMSM is given by (8) with integrated copper losses, power due to saliency and excitation.

$$P_{e-IPMSM} = \frac{3}{2} (R_s i_d^2 + R_s i_q^2 + (L_d - L_q) \omega_e i_d i_q + \omega_e \psi_f i_q) \quad (8)$$

Maximum regenerative power point currents for the IPMSM are obtained by setting the gradient of (8) to zero.

$$\left. \begin{aligned} \frac{dP_{e-IPMSM}}{di_d} &= \frac{3}{2} (2R_s i_d - L_q i_q \omega_e + L_d i_q \omega_e) \\ \frac{dP_{e-IPMSM}}{di_q} &= \frac{3}{2} (2R_s i_q + L_d i_d \omega_e - L_q i_d \omega_e + \omega_e \psi_f) \end{aligned} \right\} \quad (9)$$

At a maximum regenerative power point condition, the derivative (9) is set to zero to obtain the MRPP currents.

$$\left. \begin{aligned} \frac{dP_{e-IPMSM}}{di_d} &= \frac{3}{2} (2R_s i_d - L_q i_q \omega_e + L_d i_q \omega_e) = 0 \\ \frac{dP_{e-IPMSM}}{di_q} &= \frac{3}{2} (2R_s i_q + L_d i_d \omega_e - L_q i_d \omega_e + \omega_e \psi_f) = 0 \end{aligned} \right\} \quad (10)$$

$$\left. \begin{aligned} i_{d-min} &= \frac{-(L_d - L_q) \omega_e i_q}{2R_s} \\ i_{q-min} &= \frac{-(L_d - L_q) \omega_e i_d + \omega_e \psi_f}{2R_s} \end{aligned} \right\} \quad (11)$$

Cross-coupling component for the minimum dq-axes current in (11) can be eliminated if the q-axis current equation is substituted in the direct-axis current. The same substitution done for the d-axis gives rise to the independent dq-axes current equation as presented in (12).

$$\left. \begin{aligned} i_{d-min} &= \frac{(L_d - L_q) \omega_e^2 \psi_f}{4R_s^2 - (L_d - L_q)^2 \omega_e^2} \\ i_{q-min} &= \frac{-2R_s \omega_e \psi_f}{4R_s^2 - (L_d - L_q)^2 \omega_e^2} \end{aligned} \right\} \quad (12)$$

Substituting (12) into (8) gives rise to the maximum regenerative power as presented in (13).

$$P_{e-MRPP} = \frac{3}{2} (R_s i_{d-min}^2 + R_s i_{q-min}^2 + \omega_e \psi_f i_{q-min} + (L_d - L_q) \omega_e i_{d-min} i_{q-min}) \quad (13)$$

Braking torque equations for the SMPM and IPMSM are given in (14) and (15).

$$T_{e-SPMSM} = \frac{3P}{4} (\psi_f i_q) \quad (14)$$

$$T_{e-IPMSM} = \frac{3P}{4} (\psi_f i_q + (L_d - L_q) i_d i_q) \quad (15)$$

The maximum regenerative power point torque (MRPP-Torque) equations for the SMPM and IPMSM are obtained by substituting in (5) and (12) into (14) and (15) which gives rise to (16) and (17).

$$T_{e-SPMSM|MRPP} = \frac{-3(\psi_f^2 P \omega_e)}{8R_s} \quad (16)$$

$$T_{e-IPMSM|MRPP} = \frac{-3K_b^4 \psi_f^2 P}{8R_s} \times \frac{\omega_e}{(\omega_e + K_b)^2 (\omega_e - K_b)^2} \quad (17)$$

Where $K_b = \frac{2R_s}{L_d - L_q}$ and $P =$ pole numbers. For ease in computer simulations and accuracy, general electrical dynamic equations of the PMSM in terms of voltage, flux linkage and currents are presented in (18)-(23).

$$V_{ds} = R_s i_{ds} - \omega_e \psi_{qs} + \frac{d\psi_{ds}}{dt} \quad (18)$$

$$V_{qs} = R_s i_{qs} - \omega_e \psi_{ds} + \frac{d\psi_{qs}}{dt} \quad (19)$$

$$\psi_{ds} = \psi_f + L_{ds} i_{ds} \quad (20)$$

$$\psi_{qs} = L_{qs} i_{qs} \quad (21)$$

$$\frac{di_{ds}}{dt} = \frac{V_{ds}}{L_{ds}} - \frac{R_s i_{ds}}{L_{ds}} + \frac{L_{qs} \omega_e i_{qs}}{L_{ds}} \quad (22)$$

$$\frac{di_{qs}}{dt} = \frac{V_{qs}}{L_{qs}} - \frac{R_s i_{qs}}{L_{qs}} - \frac{L_{ds} \omega_e i_{ds}}{L_{qs}} - \frac{\omega_e \psi_f}{L_{qs}} \quad (23)$$

The general mechanical dynamic equations for the PMSM are presented in (24)-(27) respectively.

$$T_{em} = J \frac{d\omega_{mr}}{dt} + T_L + B\omega_{mr} \quad (24)$$

$$\frac{d\omega_{mr}}{dt} = \frac{1}{J} (T_{em} - T_L - B\omega_{mr}) \tag{25}$$

$$\frac{d\theta_r}{dt} = \omega_{mr} = \int \frac{d\omega_{mr}}{dt} \tag{26}$$

$$\theta_r = \int \omega_{mr} = \int \frac{d\theta_r}{dt} \tag{27}$$

The overall controlled block diagram that succinctly described the field-oriented control for the machine discussed is presented in Figure 3. A tachometer senses the mechanical speed which is converted to electrical speed. The electrical speed is then compared with a reference speed to generate a speed error. The speed error generated is tuned by a PI-controller to reduce its percentage error to a minimal value. The output of the controller serves as the d-axis reference current. Similarly, a three-phase current sensor senses the three-phase output current from the PMSM which is converted to $\alpha\beta$ two phase current using the Clarks transform.

The Parks transform is further applied to convert $\alpha\beta$ to dq-axes currents. The dq-axes currents are compared with their respective reference values to ascertain the percentage error value. The error generated is reduced with the required PI-Controller to produce the assumed dq-axes voltage which is re-transformed by the inverse Parks into three phase voltage needed in the pulse modulator. The IGBT firing signals produced from the pulse modulator is applied in switching on the inverter which controls the PMSM. The complete illustration is shown in Figure 3. The architectural block diagram of the PMSM battery powered electric vehicle (BEV) is presented in Figure 4 while the Simulink model is shown in Figure 5. The detailed analysis of different methods of regenerative braking control are presented in references [22]–[25]. The machine parameters presented in Table 1 was applied in the realization of the simulation results for the SMPM and IPMSM.

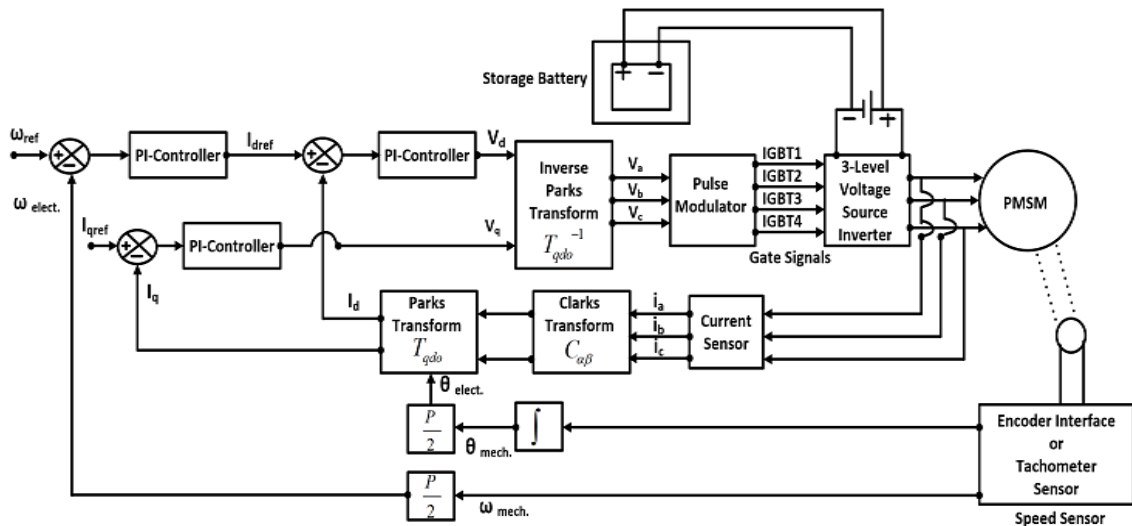


Figure 3. Overall Controlled diagram for field-oriented control scheme of PMSM

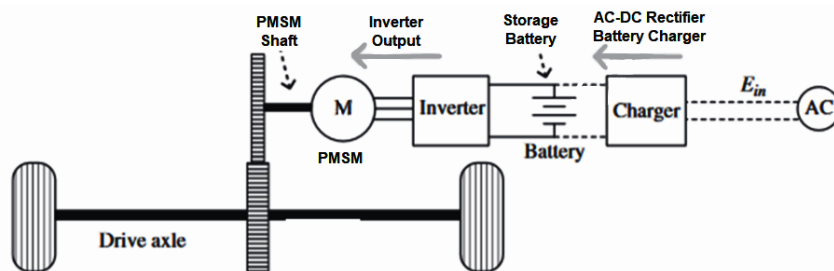


Figure 4. Diagram of PMSM operated battery powered electric vehicle

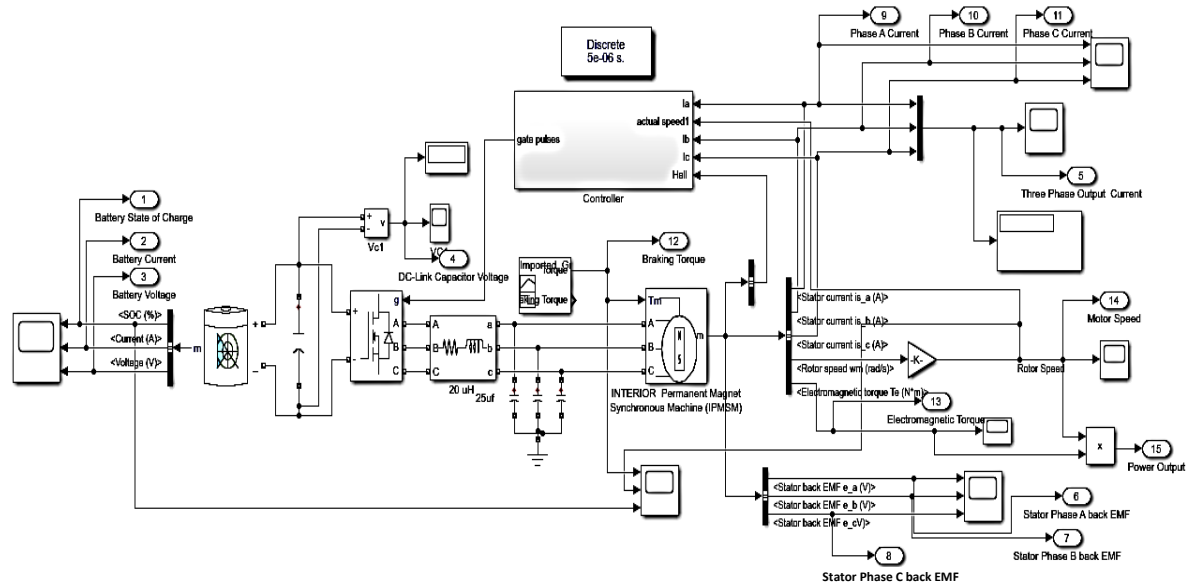


Figure 5. Simulink diagram of PMSM operated battery powered electric vehicle

Table1. Simulation parameters of PMSM and inverter used

Variable	IPMSM-machine	SPMSM-machine
Power Input (kW)	40	40
Frequency Supply (Hz)	50	50
Phase voltage (V)	400	400
Switching Frequency (KHz)	4	4
Modulation Index	0.9	0.9
Resistance of the stator (Ω)	0.0906	0.2306
direct-axis stator inductance (μH)	2080	2080
quadrature-axis stator inductance (μH)	4041	2080
Moment of inertia (Kgm^2)	0.025	0.025
Number of poles	8	8
Flux linkage (Weber.Turn)	0.107147	0.107147
Viscous friction (N.M.S)	0.0003035	0.0003035

3. RESULTS AND DISCUSSION

The plot of the active power against the q-axis current for the SMPM at varied speed is shown in Figure 6(a). It is observed that as the q-axis current increases in the positive region, the active power increases proportionately with speed whereas in the negative region the active power increases with large negative value of speed above the synchronous value of 78.55 rad per sec. In Figure 6(b), the plot of active power against dq-axes current for IPMSM at varied speed is presented in 3D-plot as against the 2D-plot in Figure 6(a). A comparative analysis of the two plots in Figures 6(a) and 6(b) proved that more active power is generated by the IPMSM than the SMPM under the same mode of operation. In Figure 7(a), the MRPP-torque for SMPM decreases as the speed increases since it is proportional to the negative value of speed as reflected in (16).

However, in Figure 7(b), the MRPP-torque of the IPMSM goes to infinity as speed increases and then assumes a large negative value after a slight reduction in speed which is in conformity with equation (17). In like manner, the slope of the maximum regenerative power in Figures 7(a) and 7(b) changes in line with the value of MRPP-torque. This implies that MRPP increases along with the electrical braking torque only if the absolute value of torque is smaller than the MRPP-torque in the regenerative region. Additionally, the total amount of regenerated energy for the IPMSM is higher than that for SMPM since it has larger MRPP-torque and maximum regenerative power point (MRPP) values. Figure 8(a) depicts the battery state of charge, the current drawn and the voltage waveforms. The state of charge decreases linearly with the constant braking torque while almost a zero current is being drawn from the battery. Inverter dc-link capacitor supplied voltage is presented in Figure 8(b) while the switching signals for the one arm inverter switches are shown in Figure 9(a). The phase and line voltages of the three-level inverter supply to the PMSM are shown in Figure 9(b). The characteristics of the auto-electric drive system on a plain surface at constant braking torque are illustrated in the simulation waveforms herein.

The three-phase output current shown in Figures 10(a) indicates that at a constant braking torque of 1.3 Nm and simulation time of 0.2016 sec., the current waveform changed in response to the change in torque and remained constant under a steady state. In Figure 10(b), the waveforms for the three phase (A, B and C) back EMF are presented. Prior to the constant braking torque, a transient rise was obtained which decreased in magnitude and retained a steady state value after a constant braking torque of 1.3 Nm. Figure 11(a) shows the constant braking torque of 1.3 Nm on a plane driving surface while Figure 11(b) presents the electromagnetic torque. It is observed that before the braking torque is applied, the electromagnetic torque rose to 3.2473 Nm due to the rise in current on no-load and decreased to -0.9809Nm while maintaining a steady state value of 1.98026 Nm at constant braking torque. The motor speed is presented in Figure 12(a). At start, the motor speed rose to 35.2195 Rad per sec and decreased to 16.5 Rad per sec at constant braking torque. The power output is presented in Figure 12(b). It is also observed that a constant power output of 32.675 kW was obtained which gave rise to a percentage efficiency value of 81.68% at a rated input power of 40 kW. Figure 13 represents the characteristic response of the battery state of charge at varied braking torque. It depicts an exponential variation during the varying torque on a sloppy driving plane. The three-phase output current is presented in Figure 14(a). It shows that the current waveforms changed in response to the varying torque producing almost twice the values obtained in Figure 10(a) during a constant braking torque. The waveforms for the three-phase back EMF are presented in Figure 14(b). It is observed that the magnitude of the back EMF increased as a result of an increased current which is in conformity with the voltage equation ($V+IR=E$) under a regenerative braking condition. The varying braking torque of the machine on a sloppy driving plane is presented in Figure 15(a) with their various values at different application time. The electromagnetic torque is also presented in Figure 15(b). It shows that at a maximum braking torque, the electromagnetic torque value of 2.204Nm was achieved. In Figure 16(a), the motor speed at a varied braking torque is presented. It is obvious that the motor speed responded swiftly to the changes in the braking torque. The waveform in Figure 16(a) is descriptive of an auto-electric drive on a sloppy plane. The power output obtained under a varying braking torque is shown in Figure 16(b). It is observed that the maximum power output generated under this condition is 29.98 kW which resulted in 74.95% efficiency at a rated power input of 40 kW. The lithium-ion battery characteristic is presented in Table 2 while the overall summary of the machine dynamic characteristics is shown in Table 3.

Table 2. Lithium-ion battery characteristics

Parameters	Value
Nominal Voltage (V)	48 V
Rated Capacity (AH)	80
Initial state of charge (%)	60
Battery response time (mS)	30
DC-DC boost converter duty cycle	0.8

Table 3. Dynamic characteristics of the machine at a varying load torque

	Driving on a plane surface	Driving on a sloppy surface
Rated power input (kW)	40	40
Maximum electromagnetic torque (Nm)	1.98026	2.204
Maximum power output (kW)	32.6752	29.98
Efficiency value (%)	81.68	74.95

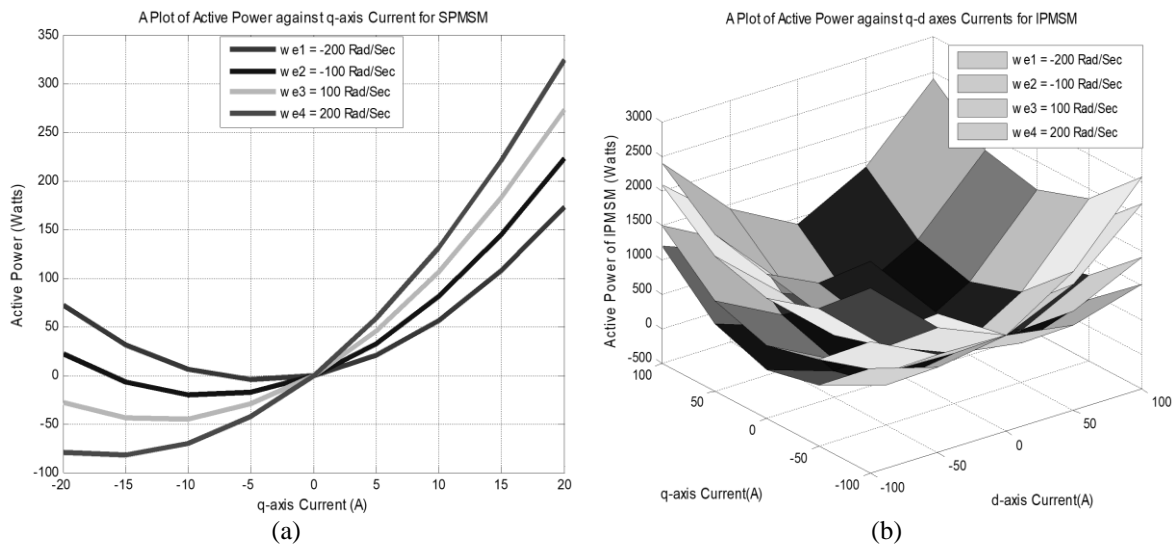


Figure 6. Active power (W) against current (A) for (a) SMPM and (b) IPMSM

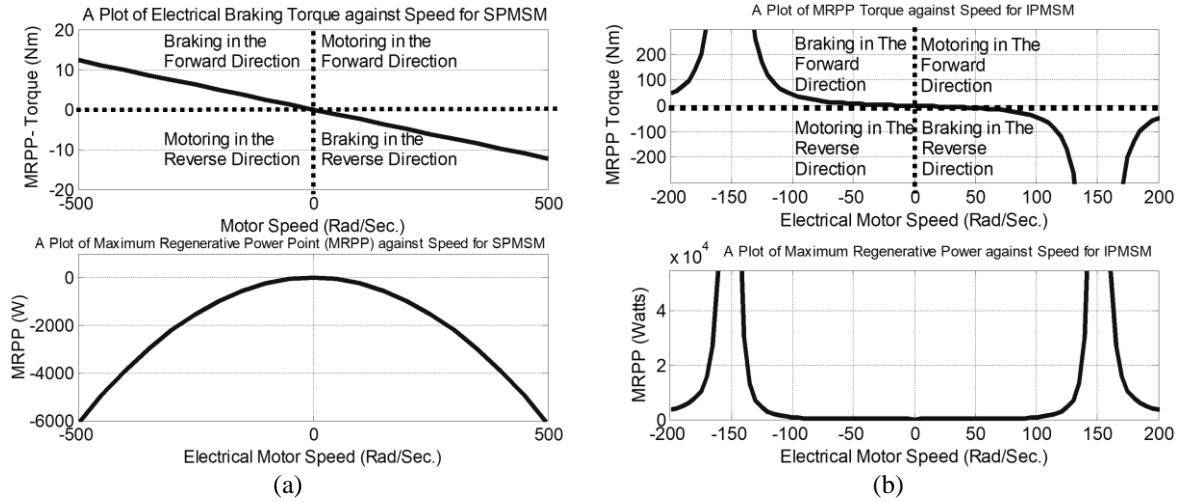


Figure 7. Torque (Nm) against speed (Rad/Sec.) for (a) SPMSM MRPP-torque and (b) IPMSM MRPP-torque

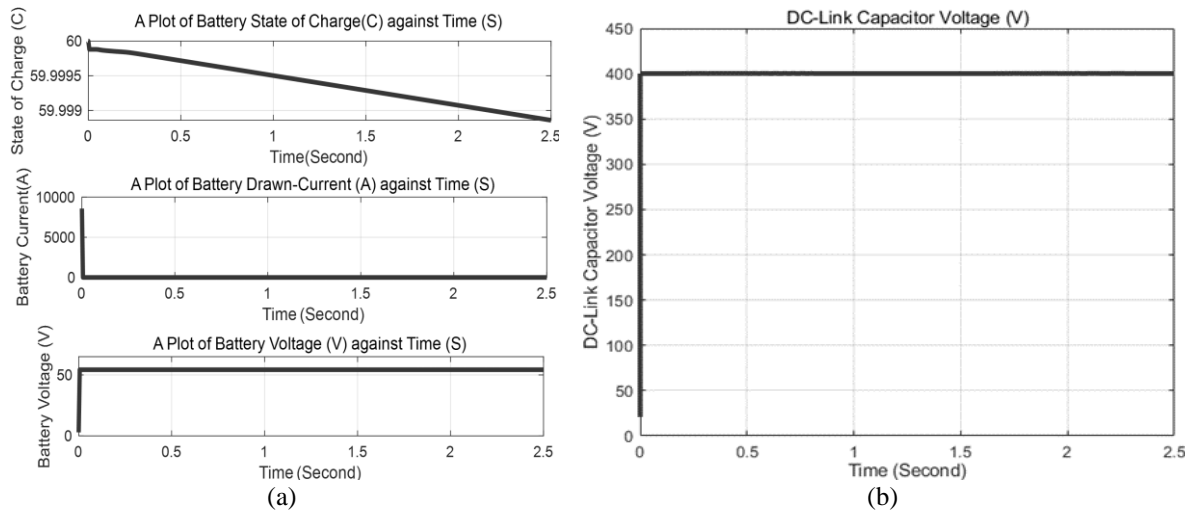


Figure 8. A Plot of (a) battery characteristic and (b) DC-link capacitor voltage (V)

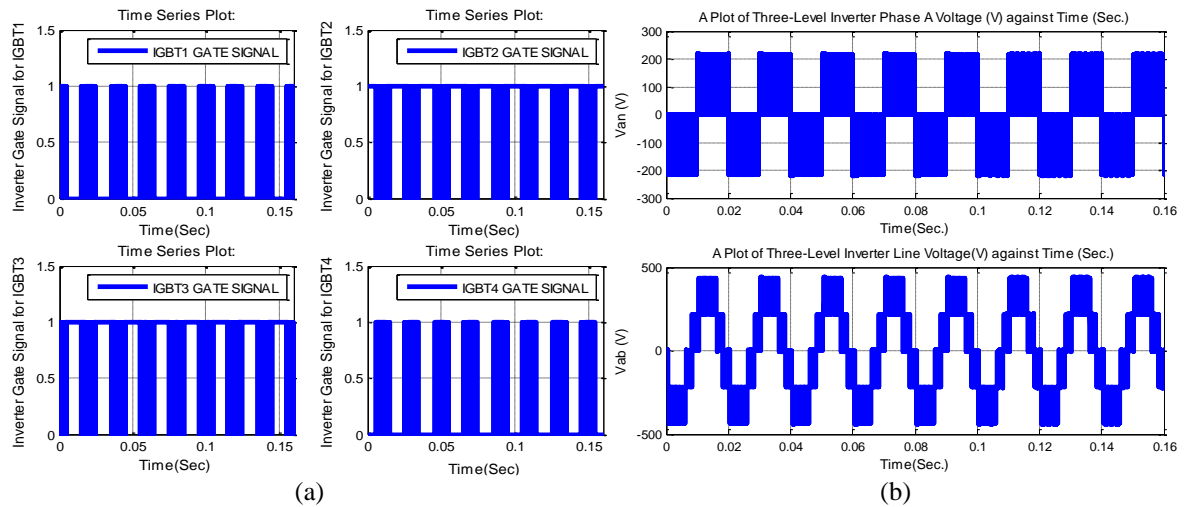


Figure 9. A plot of (a) gate signals for the inverter switches and (b) phase and line voltages of the three-level inverter

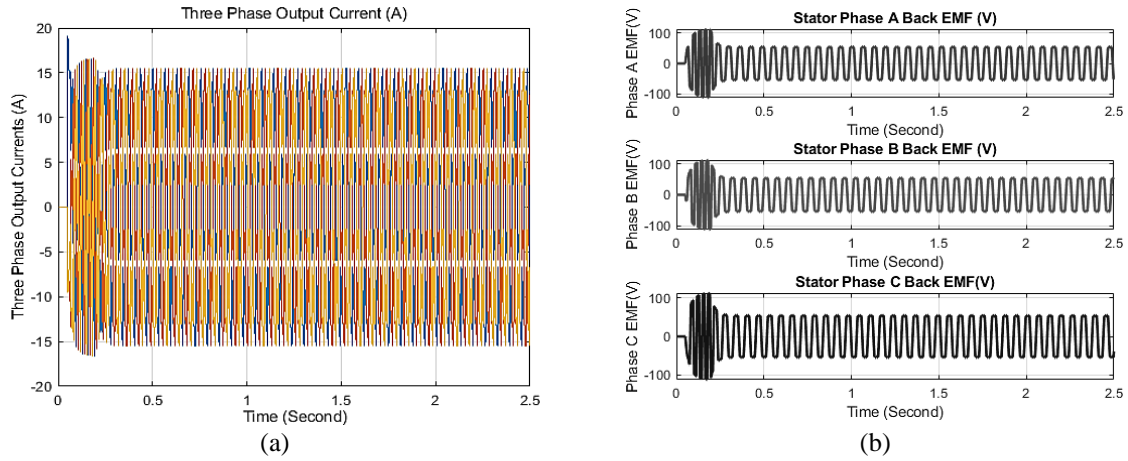


Figure 10. A Plot of (a) three phase output current (A) against time (S) and (b) three phase back EMF (V) against time (S)

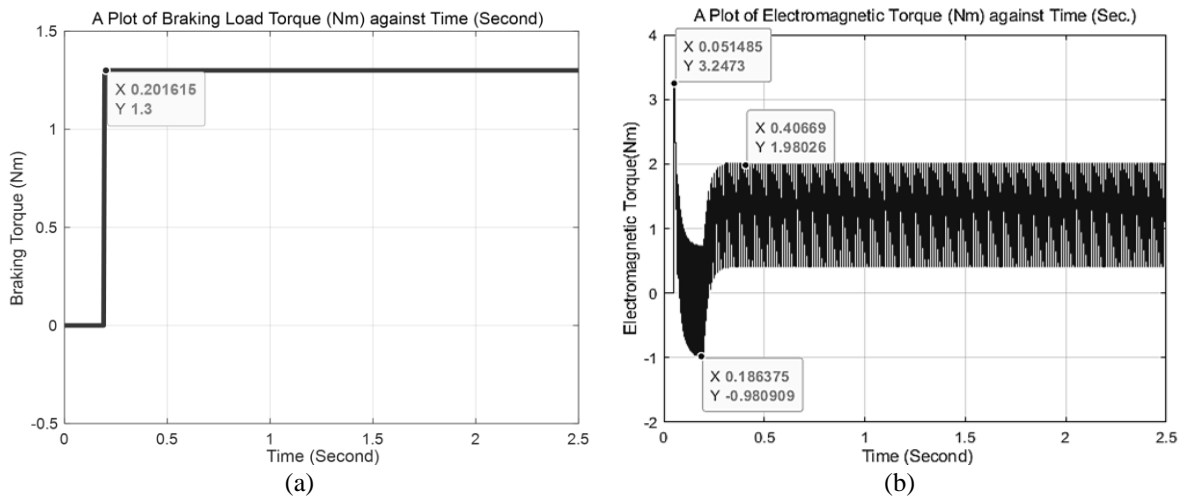


Figure 11. A plot of (a) braking torque (Nm) against time (S) and (b) electromagnetic torque (Nm) against time (S)

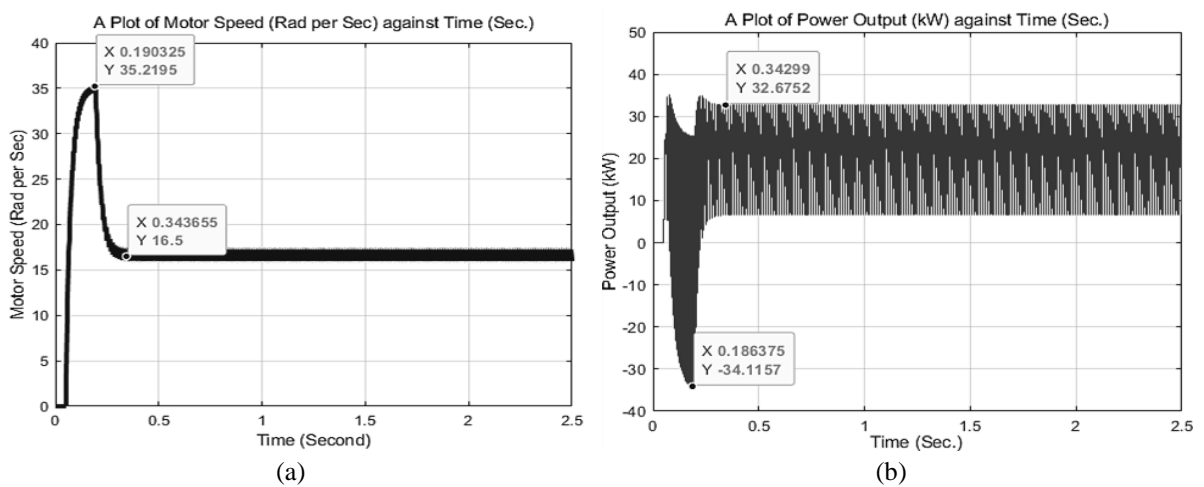


Figure 12. A plot of (a) motor speed (Rad/Sec) against time (S) and (b) power output (kW) against time (S)

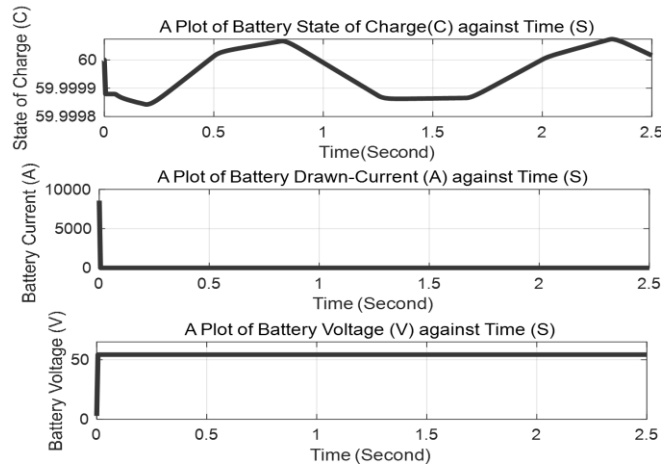


Figure 13. Plot of battery characteristic against time (S)

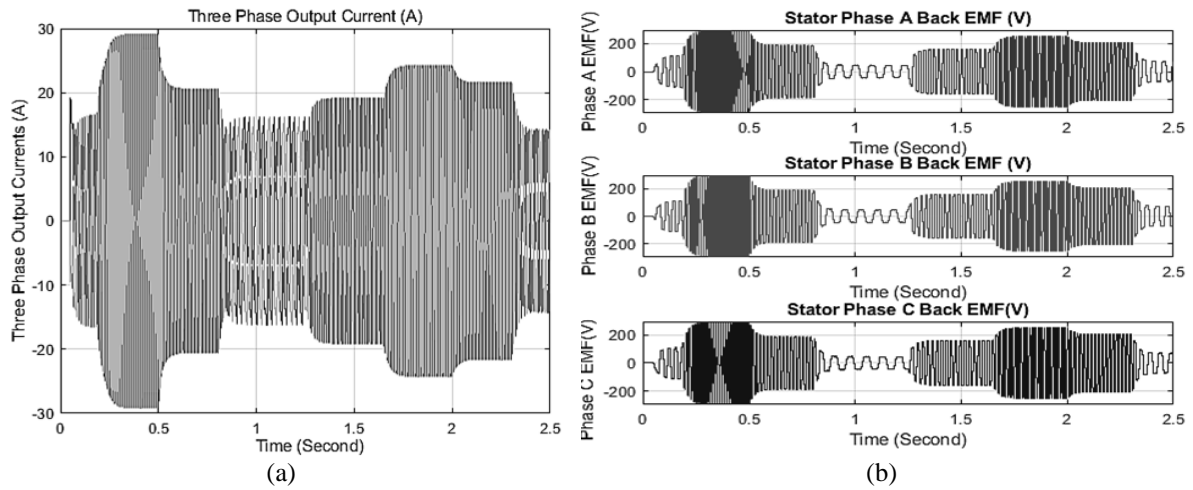


Figure 14. A plot of (a) three phase output current (A) against time (S) and (b) three phase back EMF (V) against time (S)

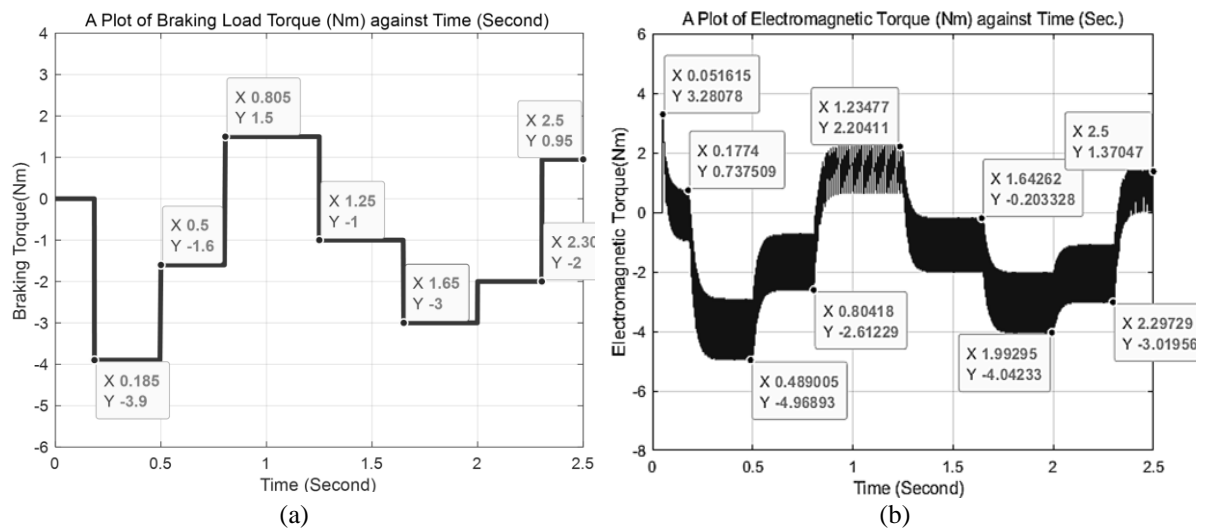


Figure 15. A plot of (a) braking torque (Nm) against time (S) and (b) electromagnetic torque (Nm) against time (S)

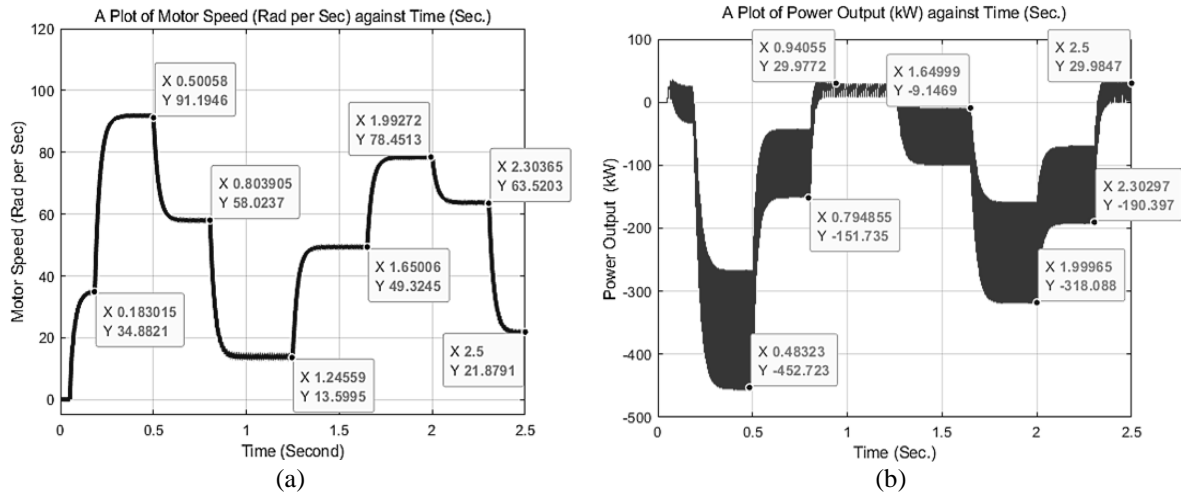


Figure 16. A plot of (a) motor speed (rad per Sec) against time (S) and (b) power output (kW) against time (S)

4. CONCLUSION

Regenerative braking in PMSM was discussed in this work and illustrated with simulations. The simulation results obtained indicated that more active power is generated by the IPMSM than the SMPM under the same operational condition. The total regenerated energy for the IPMSM is higher than that obtained for the SMPM due to the higher values in the maximum regenerative power point (MRPP) and MRPP-torque. The dynamic effects at a constant and varying braking torque on a plain and on a sloppy driving surface in terms of speed and developed torque were evaluated with simulation. Efficiency values of 81.68% and 74.95% were obtained while braking with a constant torque on level ground and with varied torque on a sloppy plane. The lithium-ion battery state of charge also decreased linearly with the constant braking torque and exponentially varied with the varying braking torque which is reflective of the variation in the efficiency values. The research findings therefore showcased the characteristic differences in running performance of the auto-electric drive at different operating surfaces which is very essential to design engineers in component selection and speed regulation. Dearth of adequate laboratory facilities formed the major limitations of the research validation and Future Scope is therefore geared towards real life implementation.




REFERENCES

- [1] C. Kuamoah, "Renewable Energy Deployment in Ghana: The Hype, Hope and Reality," *Insight on Africa*, vol. 12, no. 1, pp. 45–64, Jan. 2020, doi: 10.1177/0975087819898581.
- [2] S. Heydari, P. Fajri, N. Lotfi, and B. Falahati, "Influencing Factors in Low Speed Regenerative Braking Performance of Electric Vehicles," in *2018 IEEE Transportation Electrification Conference and Expo (ITEC)*, Jun. 2018, pp. 494–499, doi: 10.1109/ITEC.2018.8450260.
- [3] S. Heydari, P. Fajri, M. Rasheduzzaman, and R. Sabzehgar, "Maximizing regenerative braking energy recovery of electric vehicles through dynamic low-speed cutoff point detection," *IEEE Trans. Transp. Electrif.*, vol. 5, no. 1, pp. 262–270, 2019, doi: 10.1109/TTE.2019.2894942.
- [4] K. H. Nam, *AC Motor Control and Electrical Vehicle Applications*. 2018.
- [5] F. Naseri, E. Farjah, and T. Ghanbari, "An efficient regenerative braking system based on battery/supercapacitor for electric, hybrid, and plug-in hybrid electric vehicles with BLDC motor," *IEEE Trans. Veh. Technol.*, vol. 66, no. 5, pp. 3724–3738, 2017, doi: 10.1109/TVT.2016.2611655.
- [6] X. Zhang, D. Gohlich, and J. Li, "Energy-Efficient Torque Allocation Design of Traction and Regenerative Braking for Distributed Drive Electric Vehicles," *IEEE Trans. Veh. Technol.*, vol. 67, no. 1, pp. 285–295, Jan. 2018, doi: 10.1109/TVT.2017.2731525.
- [7] S. Heydari, P. Fajri, R. Sabzehgar, and M. Rasouli, "A Novel Approach for Maximizing Regenerative Braking Energy Extraction of Electric Vehicles Using Motor Performance Lookup Table," *ITEC 2019 - 2019 IEEE Transp. Electrif. Conf. Expo*, 2019, doi: 10.1109/ITEC.2019.8790633.
- [8] P. Suntharalingam, "Kinetic energy recovery and power management for hybrid electric vehicles," *Main*, vol. 57, no. 6, pp. 3428–3440, 2011, [Online]. Available: <http://dspace.lib.cranfield.ac.uk/handle/1826/6154>.
- [9] C. H. Tu, Y. C. Chang, C. L. Lin, and V. T. Liu, "Motor driving/braking control scheme with integration of multiple driving components," *Asian J. Control*, vol. 23, no. 3, pp. 1110–1120, 2021, doi: 10.1002/asjc.2417.
- [10] M. Sanada, Y. Inoue, and S. Morimoto, "Structure and Characteristics of High-Performance PMASynRM with Ferrite Magnets," *Electr. Eng. Japan*, vol. 187, no. 1, pp. 42–50, Apr. 2014, doi: 10.1002/ej.22362.
- [11] N. Mohan, *Advanced Electric Drives: Analysis, Control, and Modeling Using MATLAB/Simulink*, vol. 9781118485. 2014.




- [12] G. Tzortzis, A. Amargianos, S. Piperidis, E. Koutroulis, and N. C. Tsourveloudis, "Development of a compact regenerative braking system for electric vehicles," *2015 23rd Mediterr. Conf. Control Autom. MED 2015 - Conf. Proc.*, pp. 102–108, 2015, doi: 10.1109/MED.2015.7158736.
- [13] K. Itani, A. De Bernardinis, Z. Khatir, A. Jammal, and M. Ouedat, "Regenerative braking modeling, control, and simulation of a hybrid energy storage system for an electric vehicle in extreme conditions," *IEEE Trans. Transp. Electr.*, vol. 2, no. 4, pp. 465–479, 2016, doi: 10.1109/TTE.2016.2608763.
- [14] K. Itani, A. De Bernardinis, Z. Khatir, and A. Jammal, "Optimal traction and regenerative braking reference current synthesis for an IPMSM motor using three combined torque control methods for an Electric Vehicle," *2016 IEEE Transp. Electr. Conf. Expo, ITEC 2016*, 2016, doi: 10.1109/ITEC.2016.7520214.
- [15] S.-M. Liu, C.-H. Tu, C.-L. Lin, and V.-T. Liu, "Field-Oriented Driving/Braking Control for Electric Vehicles," *Electronics*, vol. 9, no. 9, p. 1484, Sep. 2020, doi: 10.3390/electronics9091484.
- [16] W. C. Lin, C. L. Lin, P. M. Hsu, and M. T. Wu, "Realization of anti-lock braking strategy for electric scooters," *IEEE Trans. Ind. Electron.*, vol. 61, no. 6, pp. 2826–2833, 2014, doi: 10.1109/TIE.2013.2276775.
- [17] M. K. L. C.I. Lin, C.H. Tu, *Method of adjusting Electro- Magnetic Braking Force for Electric bikes*. Taiwan: Taiwan Patent, 2018.
- [18] K. M. Choo and C. Y. Won, "Design and Analysis of Electrical Braking Torque Limit Trajectory for Regenerative Braking in Electric Vehicles with PMSM Drive Systems," *IEEE Trans. Power Electron.*, vol. 35, no. 12, pp. 13308–13321, 2020, doi: 10.1109/TPEL.2020.2994615.
- [19] S. Lim, "Sensor less-FOC with flux-weakening and MTPA for IPMSM motor Drives," *Texas Instrum. Inc. Dallas Texas*, 2018.
- [20] P. Fajri, S. Heydari, and N. Lotfi, "Optimum low speed control of regenerative braking for electric vehicles," *2017 6th Int. Conf. Renew. Energy Res. Appl. ICRERA 2017*, vol. 2017-Janua, pp. 875–879, 2017, doi: 10.1109/ICRERA.2017.8191185.
- [21] H. Gashtil, V. Pickert, D. Atkinson, D. Giaouris, and M. Dahidah, "Comparative Evaluation of Field Oriented Control and Direct Torque Control Methodologies in Field Weakening Regions for Interior Permanent Magnet Machines," in *2019 IEEE 13th International Conference on Compatibility, Power Electronics and Power Engineering (CPE-POWERENG)*, Apr. 2019, pp. 1–6, doi: 10.1109/CPE.2019.8862320.
- [22] Y. Lian, Y. Zhao, L. Hu, and Y. Tian, "Longitudinal Collision Avoidance Control of Electric Vehicles Based on a New Safety Distance Model and Constrained-Regenerative-Braking-Strength-Continuity Braking Force Distribution Strategy," *IEEE Trans. Veh. Technol.*, vol. 65, no. 6, pp. 4079–4094, Jun. 2016, doi: 10.1109/TVT.2015.2498949.
- [23] W. Xu, H. Zhao, B. Ren, and H. Chen, "A regenerative braking control strategy for electric vehicle with four in-wheel motors," in *2016 35th Chinese Control Conference (CCC)*, Jul. 2016, pp. 8671–8676, doi: 10.1109/ChiCC.2016.7554741.
- [24] G. Xu, K. Xu, C. Zheng, X. Zhang, and T. Zahid, "Fully Electrified Regenerative Braking Control for Deep Energy Recovery and Maintaining Safety of Electric Vehicles," *IEEE Trans. Veh. Technol.*, vol. 65, no. 3, pp. 1186–1198, 2016, doi: 10.1109/TVT.2015.2410694.
- [25] C. D. Xu and K. W. E. Cheng, "All-electric intelligent anti-lock braking controller for electric vehicle under complex road condition," *2016 Int. Symp. Electr. Eng. ISEE 2016*, 2017, doi: 10.1109/EENG.2016.7845986.

BIOGRAPHIES OF AUTHORS



Crescent Onyebuchi Omeje    received his Bachelor's degree in Electrical Engineering, in 2004 from University of Nigeria, Nsukka. He also obtained his Masters of Engineering (M. Eng) and Doctor of Philosophy (Ph.D) in 2011 and 2019 respectively in Electrical Engineering, from the same University. He is a Member of Nigeria Society of Engineers (MNSE), a registered member Council for the regulation of Engineering in Nigeria (COREN), a member of the Institute of Electrical/Electronic Engineering (IEEE) and a full-time lecturer in the Department of Electrical/Electronic Engineering, University of Port Harcourt, Rivers State, Nigeria. He has published widely in local and international journals. His research work focuses on power electronics, new energy conversion system, multilevel inverter applications, Electric motor drives and Power systems modeling. He can be contacted at email: crescent.omeje@uniport.edu.ng.



Candidus Ugwuoke Eya    received his B. Eng degree in Electronics Engineering, 2006 from University of Nigeria, Nsukka. He also obtained his M. Eng and Ph.D. degrees in Electrical Engineering, from the same University of Nigeria, Nsukka respectively in 2011 and 2017. He is a full-time Senior Lecturer in UNN. A member of Nigeria Society of Engineers (MNSE), registered member Council of the regulation of Engineering in Nigeria (COREN), member of IAENG. Areas of his research interests include power electronics and New energy systems applications, Multilevel inverter system, smart grid intelligent systems, condition monitoring, power electronics and Electric motor drives, control systems, parametric system applications and solar system applications. He can be contacted at email: candidus.eya@unn.edu.ng.